Vol. 01 (2025) 89-103, DOI: 10.61552/EC.2025.007

Energy Catalyst

www.jme.aspur.rs

Assessment of Dynamic Behavior of Solid Cylinders in Different Configurations under Vortex-Induced Vibrations

Seyed Reza Samaei[a,*], Mohammad Asadian Ghahfarokhi[a]

[a]*Department of Marine industries, Science and Research Branch, Islamic Azad University, Tehran, Iran.*

Keywords:

Solid cylinder, Energy harvesting, Computational fluid dynamics, Flow obstruction, Vortex, Vibrations

* Corresponding author:

Seyed Reza Samaei
E-mail: samaei@srbiau.ac.ir

Received: 4 September 2025
Revised: 29 September 2025
Accepted: 7 October 2025

ABSTRACT

The study of fluid flow around cylindrical structures presents significant challenges due to the generation of drag, lift forces, and vortex-induced vibrations (VIV), which can impact structural stability and energy harvesting applications. This research evaluates the dynamic response of solid cylinders in various configurations under VIV using computational fluid dynamics (CFD). Simulations were conducted using ANSYS Fluent with a 10 m/s inlet airflow surrounding five turbine base-like columns. A structured mesh with 63,699 independent cells ensured numerical accuracy, maintaining a mesh quality of approximately 0.8. Mass conservation reports confirm third-order accuracy, validating the computational model. The velocity vector analysis highlights flow deflection around obstacles, with localized velocity spikes reaching 22.4 m/s, in agreement with Bernoulli's principle. Contour plots of static and dynamic pressure demonstrate pressure fluctuations upon obstacle interaction, leading to vortex shedding and oscillatory forces. These fluctuations range between 48.9 and 3.98 kPa, significantly influencing the structural response. Findings indicate that VIV-induced oscillations vary with cylinder arrangement, affecting stability and fatigue life. Understanding these interactions is crucial for optimizing offshore wind turbine foundations, marine risers, and energy harvesting devices. The study contributes to the efficient design of offshore structures, reducing fatigue damage and enhancing resilience against fluid-induced vibrations.

1. INTRODUCTION

The growing global demand for renewable energy has positioned offshore wind power as one of the most promising and sustainable solutions, largely due to its superior consistency compared with onshore wind resources. However, offshore structures such as wind turbine foundations and marine risers are continuously subjected to complex hydrodynamic loading, particularly vortex-induced vibrations (VIV) — oscillatory motions arising from the unsteady interaction between fluid flow and cylindrical structural members. VIV occurs when vortices are shed alternately from opposite sides of a structure, producing fluctuating lift forces that can induce lateral oscillations. This phenomenon becomes critical when the vortex shedding frequency approaches the natural frequency of the structure, potentially leading to resonance and severe fatigue damage in components such as marine risers, cables, and mooring lines [1,2]. Consequently, understanding and mitigating VIV effects have become central topics of research across disciplines including fluid mechanics, structural dynamics, and computational fluid dynamics (CFD). As offshore infrastructure continues to expand, ensuring the long-term stability, energy efficiency, and safety of these systems requires advanced predictive modeling and improved structural design. The present study contributes to this field by analyzing multiple solid cylinders arranged in realistic offshore configurations. While most prior research has focused on single-cylinder responses, this investigation highlights the complex flow interference, vortex synchronization, and wake shielding effects that occur among multiple cylinders. Figure 1 illustrates a typical offshore wind farm, emphasizing the relevance of studying such multi-cylinder configurations in the context of marine renewable energy systems [3]. By employing CFD simulations for a five-cylinder arrangement, this study aims to provide new insights for optimizing the design of offshore wind turbine foundations, risers, and energy-harvesting devices.

Fig. 1. Example of an Offshore Wind Turbine Farm [2].

2. METHODOLOGY

2.1 Vortex-Induced Vibrations and Their Impact on Offshore Structures

Vortex-induced vibrations (VIV) are one of the primary causes of fatigue damage in offshore platforms, drilling risers, and tension leg platforms (TLPs). These slender structural elements experience complex coupled motions between the upper deck and surrounding fluid flow, resulting in relative displacements that intensify VIV phenomena [4]. At low Reynolds numbers, the flow around a cylinder remains laminar and symmetric; however, as the Reynolds number increases, asymmetry develops, and periodic vortex shedding—known as the Kármán vortex street—emerges. These alternating vortices generate fluctuating hydrodynamic forces that can excite structural oscillations in offshore pipelines and risers. The Strouhal number (St), a dimensionless parameter relating the vortex shedding frequency to the flow velocity and characteristic length of the body, governs this behavior and is expressed as:

$$St = \frac{f_{st} D}{U} \tag{1}$$

where f_s is the vortex shedding frequency, D is the cylinder diameter, and UUU denotes the free-stream flow velocity. For circular cylinders, the Strouhal number typically remains around 0.2 over a wide range of flow regimes [5]. When the shedding frequency coincides with the structural natural frequency, resonance occurs, amplifying vibrations and accelerating fatigue damage. In terrestrial conditions, wind velocity profiles are influenced by surface roughness within the atmospheric boundary layer. The variation of wind velocity with height can be approximated using the power-law relation:

$$V_Z = V_g\left(\frac{Z}{Z_g}\right)^{a} \tag{2}$$

where V_g is the gradient wind speed, Z_g is the height of the gradient layer, and a is the power exponent, ranging from about 0.15 for open terrains to 0.5 for dense urban areas [6]. Beyond its detrimental effects, VIV can also be exploited for energy harvesting, as oscillating cylinders provide a means of converting flow-induced motion into electrical power through piezoelectric or electromagnetic mechanisms [7,8]. Understanding these dual aspects—damage and potential benefit—offers a comprehensive foundation for improving offshore resilience and sustainability.

2.2 Wind Effects and Structural Response to Vortex Formation

In standard wind engineering practice, the reference wind speed is measured at a height of 10 meters above ground level, typically over flat and unobstructed terrain. The probability of this speed being exceeded within a 50-year return period is generally less than 2% [9]. When a moving air stream encounters an obstacle, it divides and flows around the structure, rejoining on the leeward side where turbulence forms as the velocity increases. On the windward side, positive (stagnation) pressure is generated, while the leeward face experiences negative pressure (suction) due to vortex shedding. As wind speed increases, these vortices also induce fluctuating suction forces along the side surfaces. The periodic nature of these rotational flows causes oscillations in both the along-wind and across-wind directions. When the frequency of these aerodynamic excitations coincides with the natural frequency of the structure, resonance occurs, amplifying dynamic pressures and potentially compromising structural stability [10]. Understanding such aerodynamic interactions is essential for the design of wind-resistant and vibration-tolerant structures. Figure 2 illustrates the pressure distribution generated by wind flow around a typical obstacle, highlighting regions of positive and negative pressure that led to oscillatory motion [11].

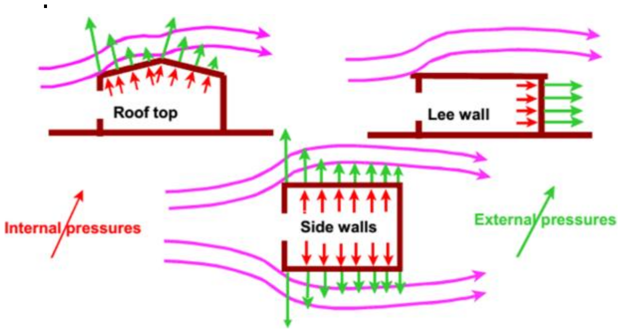

Fig. 2. Wind-induced pressure around a structural obstacle [11].

Wind force is inherently variable, exerting different magnitudes on structures depending on elevation above sea level. The mean wind velocity profile is therefore used to represent an average condition. Although the magnitude of wind force is relatively small compared with other external loads, it generates significant moments at the base of tall or slender structures [12]. The general form of the wind force per unit area can be expressed as:

$$F = C_{D_2}\frac{\rho D}{2}\left|\left(\frac{h'}{h}\right)^{\frac{1}{n}}\bar{u}(h)\right|\left(\frac{h'}{h}\right)^{\frac{1}{n}}\bar{u}(h) \quad (3)$$

where C_D is the drag coefficient, ρ is the air density, D is the reference dimension, h is the reference height, h′ is the evaluation height, n is the power-law exponent, and $\bar{u}(h)$ represents the mean wind velocity at height h. As discussed earlier, wind energy remains one of the most abundant and sustainable natural resources, with a global potential exceeding 25,000 GW. Harnessing this energy enables the operation of wind turbines that supply a significant share of the world's mechanical and electrical demand without producing greenhouse gases. Although the manufacturing and maintenance of wind turbines require advanced technology, their installation and commissioning are considerably faster and simpler than conventional fossil-fuel-based power plants. Recent studies indicate that a 5.1 MW wind turbine can generate approximately 4 million kWh per year, preventing the emission of nearly 1 million tons of CO_2 annually [13]. Figure 3 demonstrates the worldwide growth trend in wind energy production between 2000 and 2015.

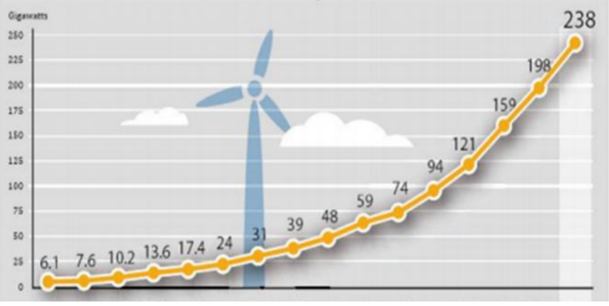

Fig. 3. Annual growth in global wind power generation, 2000–2015 [13].

Iran, with a land area of about 1,648,000 km^2, extends between longitudes 44° E–64° E and latitudes 25° N–40° N. More than half of the country is mountainous, resulting in diverse climatic conditions. The eastern and southeastern regions experience arid climates with considerable diurnal temperature variations. Despite the limited number of high-wind zones, several regions exhibit favorable potential for wind power development. According to the national wind atlas, illustrated in Figure 4, the estimated nominal capacity of identified sites reaches nearly 60,000 MW, while the extractable wind energy potential using current turbine technology exceeds

18,000 MW [14]. These statistics underscore Iran's strategic capability to expand its renewable energy sector, particularly in the domain of offshore and high-altitude wind farms.

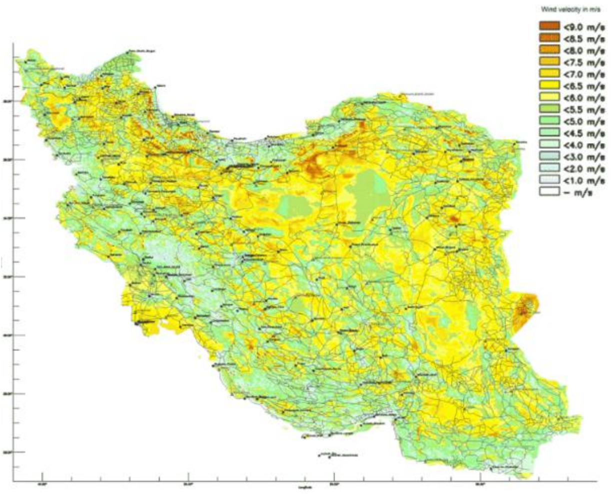

Fig. 4. Wind atlas of Iran, highlighting regional potential for wind energy development [14].

2.3 Wind Energy Potential and Modern Turbine Capabilities

Estimates of wind energy potential have traditionally relied on conventional turbine parameters; however, the deployment of advanced technologies such as the EnelX generation of modern turbines has demonstrated that the effective capacity can nearly double under similar wind conditions [15]. This significant increase underscores Iran's vast potential for wind power development, even when evaluated using traditional turbine designs.

Despite the technical potential, the expansion of Iran's wind energy sector has been limited by the high initial cost of conventional turbine systems. A case in point is Zahedan, a southeastern city with a population exceeding 550,000, which exhibits one of the most favorable wind profiles in the country. Situated at 60°51′25″ E and 29°30′25″ N, Zahedan records an average annual wind speed of 5.05 m/s at a height of 50 m above sea level. Table 1 presents the average monthly wind speed variations for the Zahedan site, derived from the national wind atlas. These data highlight the seasonal consistency of wind resources in the region, suggesting that Zahedan could serve as a benchmark for small-to-medium-scale wind power deployment [16].

Table 1. Average monthly wind speed at Zahedan site (m/s) at 50 m height [16].

Wind Speed (m/s)	Month	Wind Speed (m/s)	Month
7.4	Mehr	7.4	Farvardin
5.5	Aban	6.5	Ordibehesht
4.3	Azar	5.2	Khordad
4.3	Dey	8.2	Tir
4.3	Bahman	8.0	Mordad
7.4	Esfand	8.1	Shahrivar

Average annual speed = 5.05 m/s

Offshore construction environments pose unique challenges arising from the combined effects of fluid currents and wind loads, which require precise fluid dynamic analyses to ensure structural stability [17]. Cylindrical offshore elements—such as piles, risers, and turbine columns—are particularly susceptible to aerodynamic inefficiencies. High Reynolds numbers in these settings produce turbulent flow patterns, resulting in drag, lift, and cyclic fatigue loading. In offshore environments, slender columns and risers undergo oscillatory motion, and their interaction with surrounding flow fields intensifies stress concentrations. When the vortex shedding frequency matches the structure's natural frequency, resonance may occur, amplifying oscillations and accelerating fatigue in pipelines and risers [18]. The nonlinear nature of these fluid–structure interactions (FSI) necessitate advanced numerical approaches to accurately capture vortex behavior [19]. The present study employs computational fluid dynamics (CFD) using Gambit for mesh generation and ANSYS Fluent for flow simulation. Both single- and multi-cylinder configurations are analyzed to understand the mechanisms of vortex-induced vibrations (VIV) relevant to marine pipelines, bridge piers, and heat exchangers [20]. Tandem-cylinder arrangements introduce additional boundary layer complexities that alter separation points and overall flow physics. Historical milestones in offshore wind energy further contextualize this research. The concept of offshore wind generation originated in 1930, while William Heronemus of MIT advanced the first modern design framework in 1972. The first offshore wind turbine, rated at 230 kW, was installed in 1990 approximately 250 m off the coast of Sweden at a depth of 7 m [21]. Figure 5 depicts one of the early global prototypes of offshore wind turbines.

Fig. 5. Early offshore wind turbine prototype [21].

The world's first offshore wind farm, comprising 11 turbines with a combined capacity of 5 MW, was commissioned in 1991. Three years later, the Netherlands launched a 2 MW farm, marking the start of broader European expansion. By 2003, international momentum had accelerated, with several countries investing heavily in offshore wind technology. For example, Ireland's facility—illustrated in Figure 6—consists of seven turbines, each rated at 6.3 MW [22].

Fig. 6. Offshore wind farm in Ireland [22].

The largest offshore installation to date, shown in Figure 7, is located in Denmark and features 80 turbines totaling 160 MW, situated 14–20 km from the coastline [23].

Fig. 7. Offshore wind farm in Denmark with 160 MW capacity [23].

Recent innovations have introduced deep-sea turbines, including Norway's Hywind (Figure 8) and the Netherlands' BlueH system (Figure 9), with rated powers of 2 MW and 3 MW, respectively. These units are designed for greater ocean depths and extended offshore distances [24].

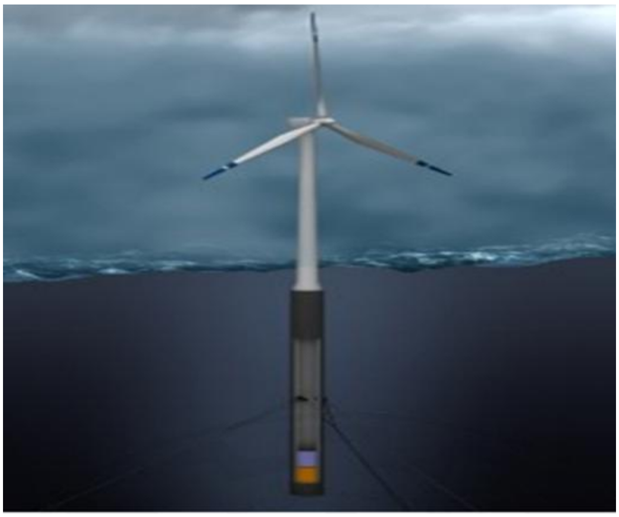

Fig. 8. Schematic of the Hywind floating turbine [24].

Fig. 9. BlueH offshore turbine concept [24].

In recent years, numerous studies have significantly advanced the understanding of vortex-induced vibrations (VIV) in marine and offshore structures. The VIV behavior of a single spherical body under low Reynolds numbers was analyzed in [25], while other works focused on isolated cylindrical structures [26,27]. Only a limited number of investigations have addressed tandem-cylinder interactions, where the downstream cylinder is positioned within the wake of the upstream one. Studies such as [28,29] demonstrated that the spacing ratio (S/D) between cylinders strongly affects flow interference patterns, vortex synchronization, and vibration amplitudes. Experimental research [30] revealed that the shielding effect produced by the leading cylinder reduces the mean drag force acting on the trailing one, though this effect diminishes as the S/D ratio increases. Similar observations were reported in [31-33], confirming that multiple-cylinder arrangements produce complex, periodic flow structures governed by wake merging and reattachment phenomena. Complementary regional analyses [34] quantified long-term wind characteristics across Iranian cities such as Sabzevar, establishing local wind regimes and estimating wind energy density at various elevations. These results emphasized the role of seasonal variations in wind speed and direction in determining viable turbine deployment locations. Figure 10 schematically presents the distribution of internal and external aerodynamic forces acting on a structure exposed to wind.

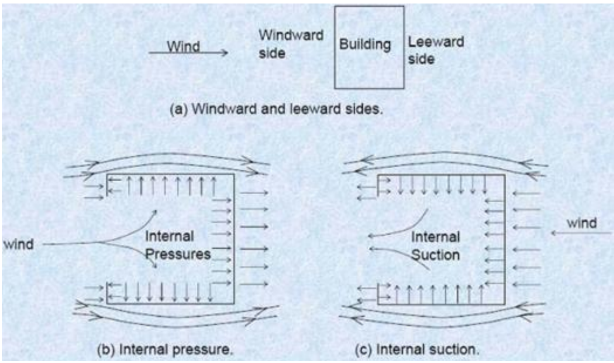

Fig. 10. Internal and external wind forces on a structural system [34].

Additional statistical studies [35] reinforced the suitability of several Iranian and regional locations for wind energy generation, employing Weibull and Rayleigh probability functions to model long-term power output. Further investigations expanded these findings through economic feasibility and site-selection analyses, while more recent optimization research explored aerodynamic improvements such as Gurney flaps and vortex generators, which can enhance turbine performance by up to 20% under optimal conditions. Building on this knowledge base, the present study integrates CFD-based hydrodynamic modeling with site-specific design validation for chain-type modular floating docks at Bahonar Port. Unlike earlier studies focused solely on rigid pontoons or conventional breakwaters, this research combines geometric optimization, fluid–structure interaction (FSI) analysis, and environmental validation, resulting in a practical and innovative approach to offshore infrastructure design. Figure 11 summarizes the distribution of aerodynamic and hydrodynamic forces acting on a horizontal-axis wind turbine.

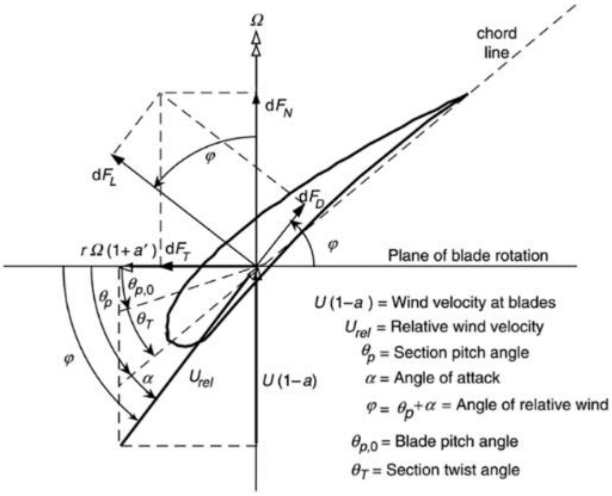

Fig. 11. Distribution of aerodynamic and hydrodynamic forces on a horizontal-axis wind turbine.

To ensure accurate aerodynamic assessment, this study also refers to wind tunnel testing, a crucial technique for replicating airflow behavior and measuring aerodynamic performance. Figure 12 illustrates a NASA wind tunnel test, showing airflow streamlines and pressure zones around a scaled model aircraft.

Fig. 12. NASA wind tunnel test showing flow characteristics around a model aircraft.

Modern wind tunnels are composed of several sections—including an inlet, honeycomb flow straighteners, contraction chamber, test section, and diffuser—that collectively maintain stable and uniform airflow. Figure 13 depicts the structural layout of a standard aerodynamic wind tunnel, and

Figure 14 shows the airflow circulation process in a closed-circuit configuration. These facilities enable high-precision testing of aircraft, vehicles, and offshore structural components, although they require sophisticated instrumentation and rigorous safety standards.

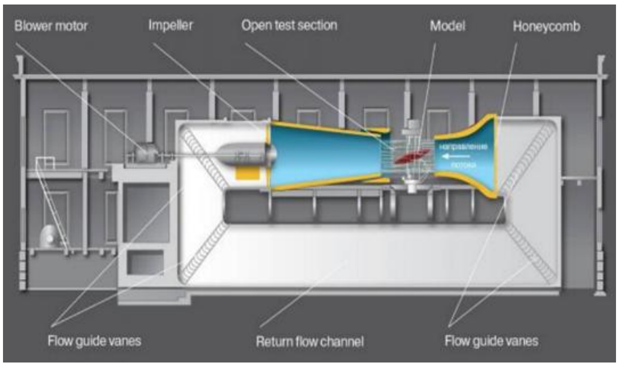

Fig. 13. Cross-section of a standard aerodynamic wind tunnel.

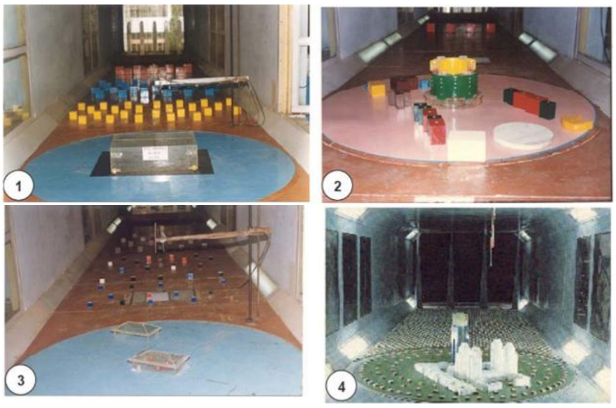

Fig. 14. Airflow circulation in a closed-circuit wind tunnel used for aerodynamic testing.

The five-cylinder configuration adopted in this study replicates realistic offshore conditions such as turbine foundations and jacket piles. The spacing ratios (S/D = 2–4) were selected based on validated experimental research, ensuring accurate capture of wake interference effects and reliable comparison with prior findings.

3. RESULTS

The numerical simulations were carried out in ANSYS Fluent, using Gambit software for mesh generation and domain configuration. The modeled geometry consisted of five symmetrically arranged columns, representing clustered offshore support structures such as turbine bases. The computational domain included the surrounding air volume and precise column coordinates to ensure accurate fluid–structure interaction modeling. A structured mesh with 63,699 cells, 147,318 faces, and 22,910 nodes was generated and distributed across four partitions to optimize computational speed. The minimum orthogonal quality of the grid was 0.0779, and the maximum aspect ratio was 40.26, confirming good mesh uniformity. Figure 15 shows the geometry of the modeled five-column configuration created in Gambit, including the symmetry planes used to reduce computational cost and ensure numerical stability.

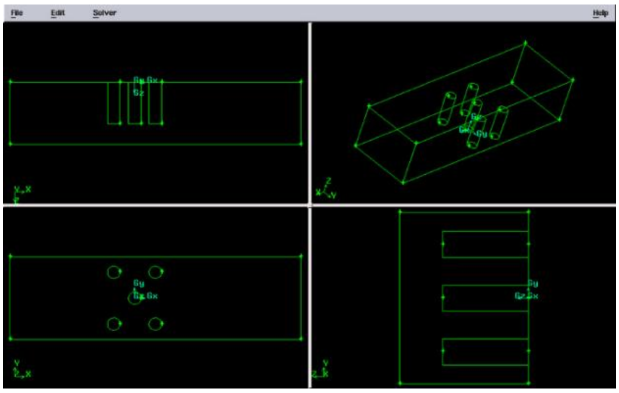

Fig. 15. Geometry of the five-column configuration modeled in Gambit.

Boundary conditions were defined as follows: an inlet velocity of 10 m/s, an outlet pressure condition, and no-slip wall boundaries. The working fluid was air at standard atmospheric conditions. Figure 16 illustrates the imposed boundary conditions and the meshed domain layout.

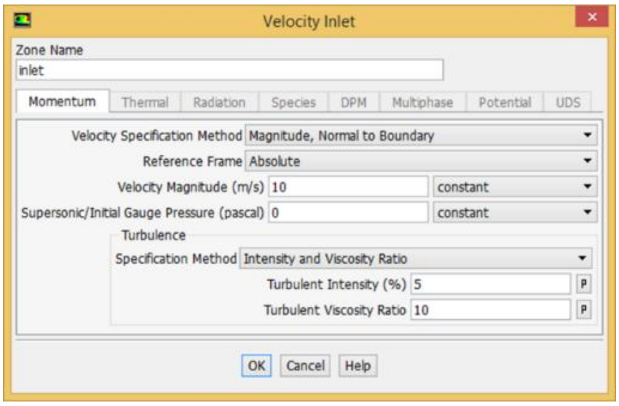

Velocity Inlet

Zone Name: inlet

Velocity Specification Method: Magnitude, Normal to Boundary

Reference Frame: Absolute

Velocity Magnitude (m/s): 10 constant

Supersonic/Initial Gauge Pressure (pascal): 0 constant

Turbulence

Specification Method: Intensity and Viscosity Ratio

Turbulent Intensity (%): 5

Turbulent Viscosity Ratio: 10

Fig. 16. Applied boundary conditions and domain layout.

The realizable k–ε turbulence model was used as the closure model, as it provides reliable performance for bluff-body flow simulations under subcritical Reynolds regimes.

Second-order upwind schemes were employed for the discretization of momentum, pressure, and turbulence transport equations.

Pressure–velocity coupling was handled using the SIMPLEC algorithm, with a residual convergence criterion of 1×10^{-5}. To evaluate numerical independence, several mesh resolutions were tested by gradually refining the grid and analyzing the effects on velocity and pressure gradients.

Contour plots of longitudinal and transverse planes were used to study local flow variations and turbulence intensity around the columns. The simulations yielded three main outcomes:

1. noticeable flow deflection and velocity amplification behind the leading cylinders,
2. significant pressure fluctuation across downstream cylinders, and
3. variation in vortex-induced vibration (VIV) response based on cylinder arrangement.

3.1. Mesh Independence and Model Validation

To verify numerical accuracy, a mesh independence test was conducted by progressively refining the grid from 63,699 cells to 255,000 cells. Beyond 120,000 cells, changes in the aerodynamic coefficients (C_d, C_l, and S_t) remained below 2%, confirming grid convergence. Validation was performed by comparing results from a single-cylinder model at Re ≈ 10^4 with experimental data reported. The computed lift and drag coefficients differed by less than 6%, and the Strouhal number matched within ±0.01, verifying the reliability of the CFD setup. Flow visualization was used to observe turbulence intensity and vortex formation.

Figure 17 presents the turbulence contours around the five-column array, highlighting high-intensity regions in the wake zones, especially downstream of the central and outer columns.

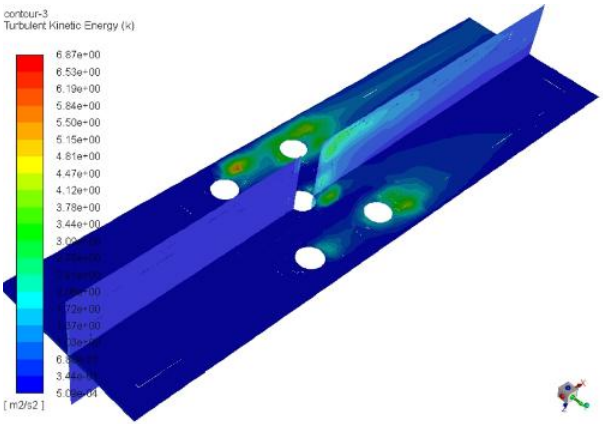

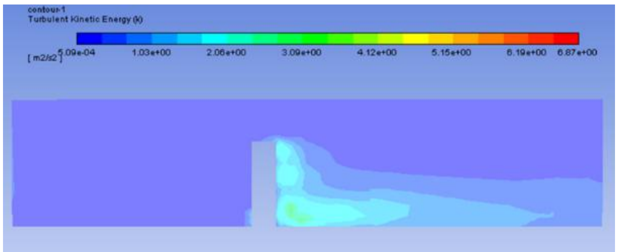

Fig. 17. Turbulence intensity contours around the columns.

3.2. Static and Dynamic Pressure Fields

The variation of static pressure over the column surfaces is illustrated in Figure 18, showing pressure concentration on the windward sides and suction zones on the leeward sides. These results indicate the asymmetrical distribution of pressure that contributes to vortex shedding and unsteady lift forces. To better understand vortex formation, velocity vectors were analyzed in three-dimensional space. Figure 19 shows the 3D velocity vector field, where strong rotational patterns appear behind the columns, demonstrating the formation of distinct vortices in alternating directions.

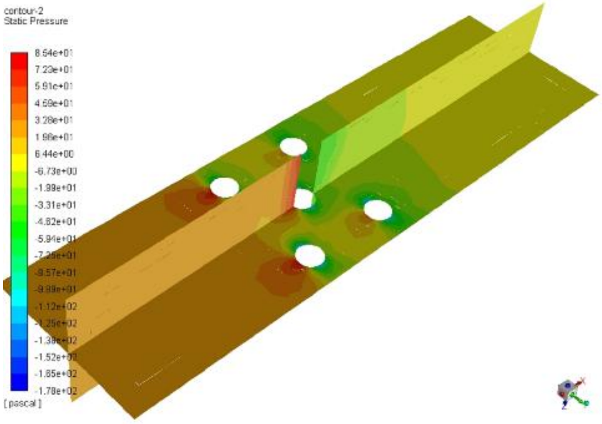

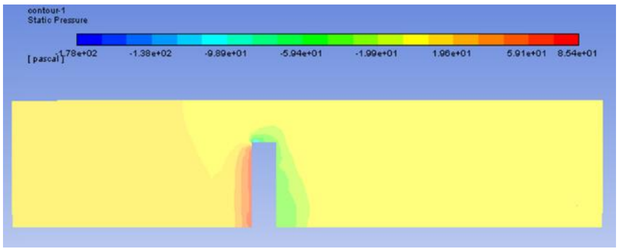

Fig. 18. Static pressure distribution on column surfaces.

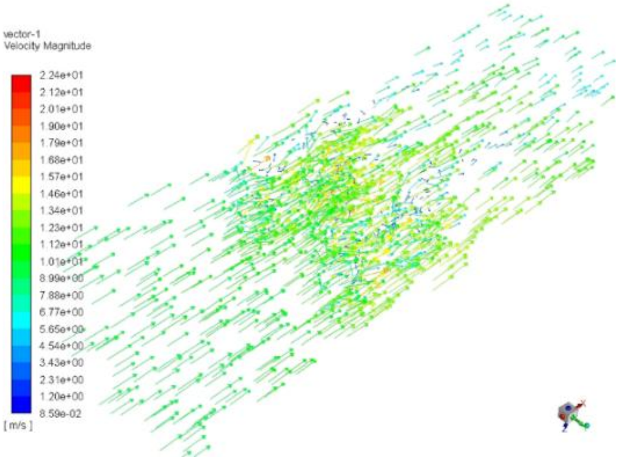

Fig. 19. Three-dimensional velocity vectors showing wake rotation.

The magnitude of velocity changes is shown in Figure 20, revealing areas of accelerated flow between cylinders and reduced velocity regions downstream.

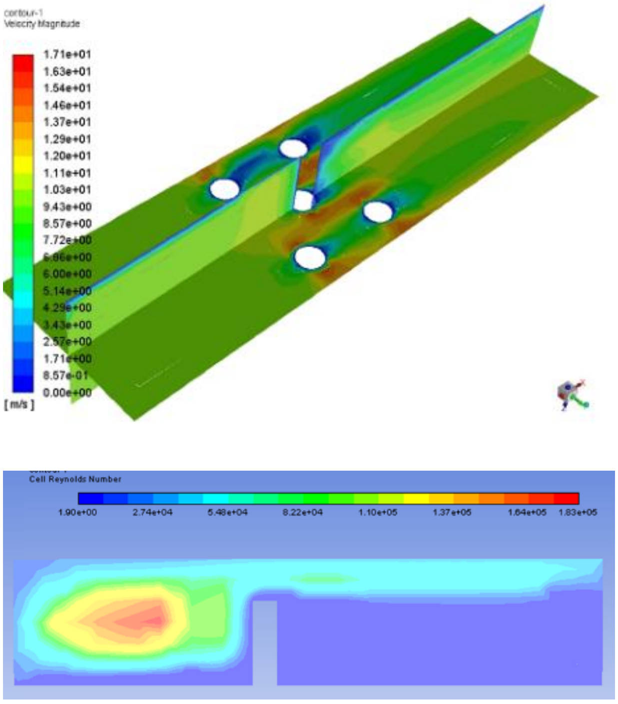

Fig. 20. Velocity magnitude contours around columns.

The dynamic and total pressure contours are presented in Figure 21, which display localized low-pressure cores in the wake and high-pressure zones between the columns, confirming alternating flow-induced loads.

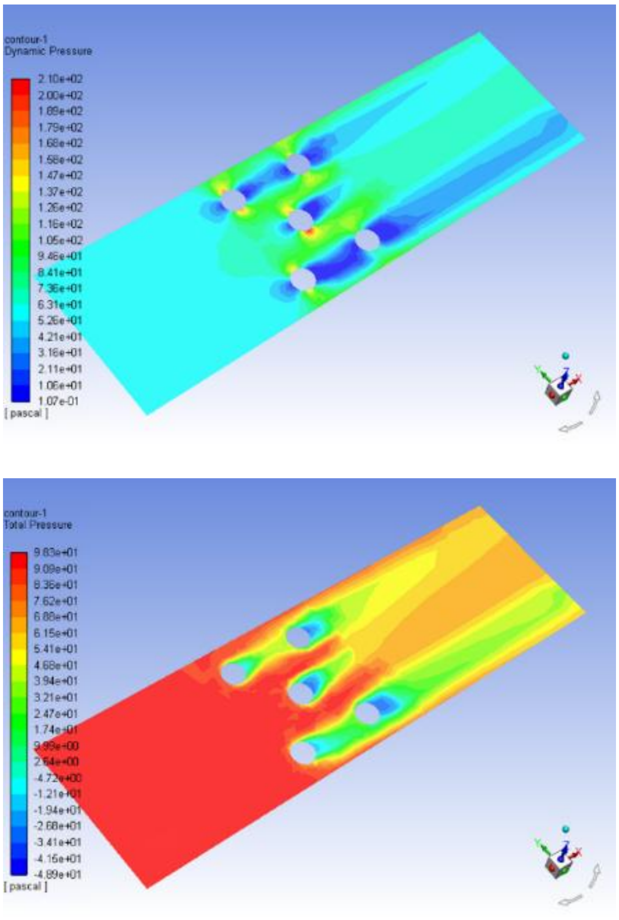

Fig. 21. Dynamic and total pressure contours in the wake region.

The computed Reynolds number distribution (Figure 22) identifies the transitional regions between laminar and turbulent zones, confirming a subcritical flow regime throughout the domain.

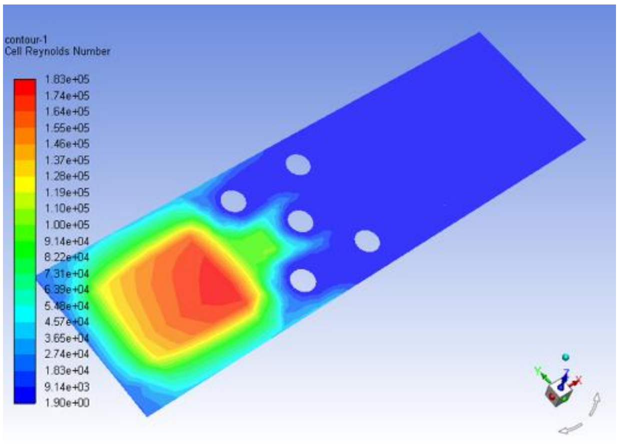

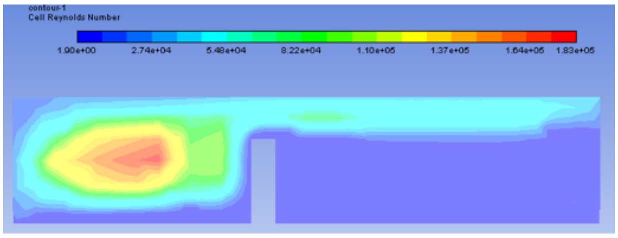

Fig. 22. Reynolds number distribution across the flow field.

3.3. Velocity Components and Flow Profiles

To quantify directional flow variations, tangential, axial, and radial velocity components were extracted along multiple cross-sections.

Figure 23 displays the tangential velocity, indicating alternating circulation directions typical of vortex shedding patterns.

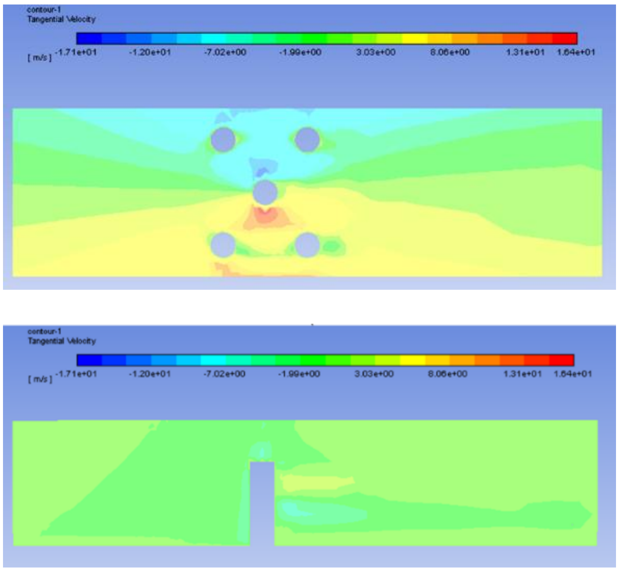

Fig. 23. Tangential velocity distribution along the cylinder array.

Figure 24 presents the axial velocity profile, showing delayed recovery of the flow field behind the leading cylinders due to shielding effects.

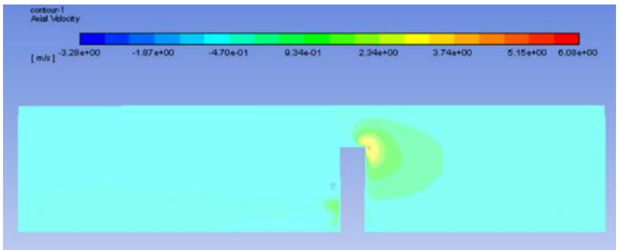

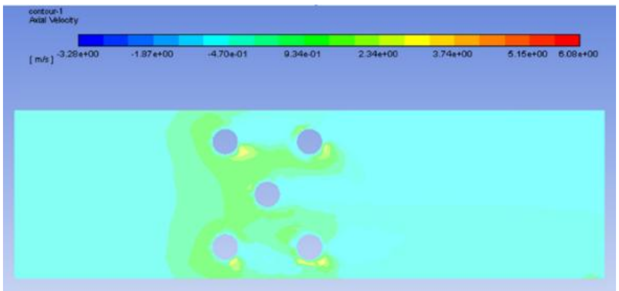

Fig. 24. Axial velocity profile downstream of columns.

Figure 25 illustrates the radial velocity contours, highlighting the magnitude of cross-stream momentum transfer between cylinders.

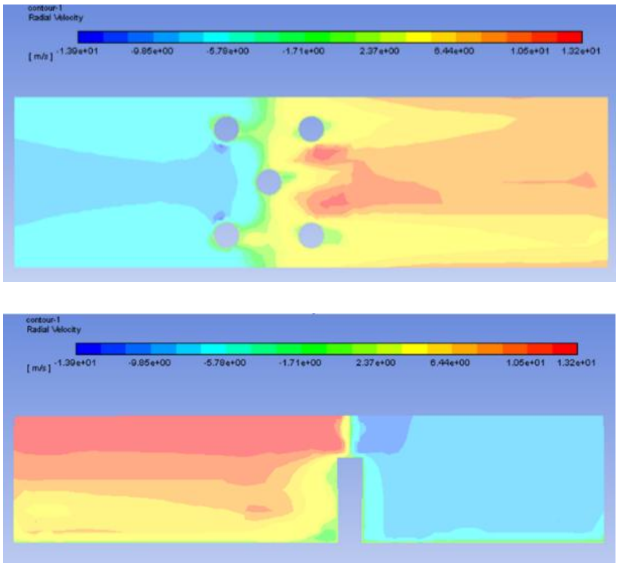

Fig. 25. Radial velocity distribution around the columns.

To analyze longitudinal trends, Figure 26 depicts the static pressure profile along the x-axis, demonstrating the gradual pressure recovery behind the leading cylinder.

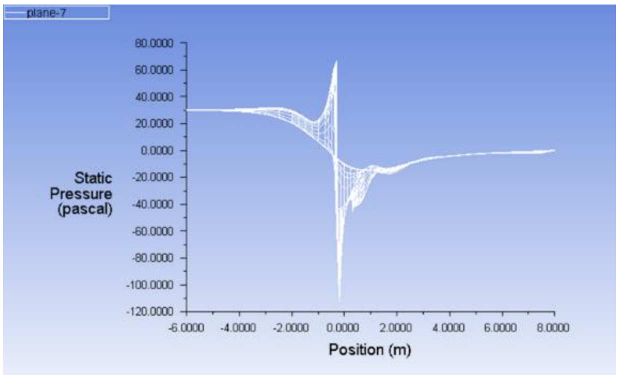

Fig. 26. Longitudinal static pressure profile along the x-axis.

Similarly, Figure 27 shows the velocity profile along the same axis, emphasizing the downstream velocity deficit and gradual reattachment of the flow.

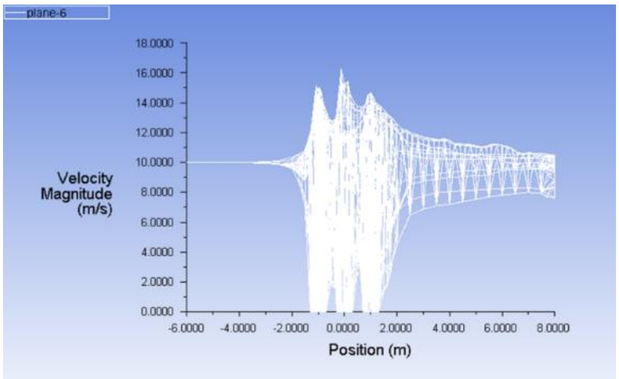

Fig. 27. Streamwise velocity profile along the x-axis.

3.4. Mass Conservation and Force Evaluation

The mass flow rate at the inlet and outlet boundaries was compared to ensure global mass conservation. The results, summarized in Table 2, confirm negligible mass imbalance, validating solver stability and boundary condition accuracy.

Table 2. Inlet and outlet mass flow rates.

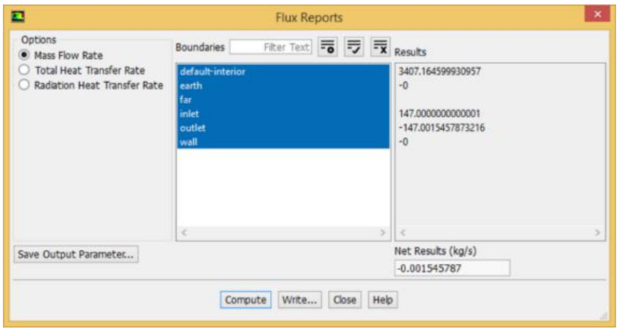

Boundaries	Results
default-interior	3407.164599930957
earth	-0
far	
inlet	147.0000000000001
outlet	-147.0015457873216
wall	-0

Net Results (kg/s)
-0.001545787

The total hydrodynamic forces acting on the structure were also calculated.

The analysis revealed that pressure forces dominate over viscous shear, with a total wall force of 505.03 N and a net force of 309.33 N in the primary flow direction (1,0,0).

These findings confirm that pressure fluctuations play a major role in the flow-induced vibration behavior of clustered offshore columns. Figure 15 (geometry) and Figure 16 (boundary setup) provide the fundamental context for the applied CFD domain, while the subsequent figures (17–27) sequentially visualize turbulence intensity, pressure distribution, velocity components, and flow recovery, leading to a comprehensive understanding of hydrodynamic performance.

Finally, the refinement study up to 255,000 cells confirmed that the mesh with 120,000 cells offers an optimal balance between accuracy and computational efficiency.

4. DISCUSSION

The numerical findings presented in this study provide a detailed understanding of the fluid–structure interaction mechanisms governing flow behavior around clustered cylindrical obstacles.

The CFD simulations revealed how variations in cylinder spacing, arrangement, and flow direction directly influence vortex formation, pressure fluctuations, and induced vibration response. The five-cylinder configuration effectively demonstrated the transition from isolated-cylinder flow to complex wake interference patterns, validating the model's capability to capture coupled hydrodynamic effects in realistic offshore conditions. A key observation was the velocity amplification behind the leading cylinders, where flow acceleration occurred due to reduced cross-sectional area. This observation is consistent with Bernoulli's principle, which predicts an increase in velocity in constricted flow paths, followed by a corresponding pressure drop.

These accelerated jets generated high shear regions, which in turn promoted the formation of alternating vortices in the downstream wake.

The turbulence intensity contours indicated strong vortex roll-up and dissipation, highlighting the interplay between inertial and viscous forces within the wake zone.

This behavior was especially evident in the tandem and staggered column interactions, where flow deflection from the upstream cylinder imposed periodic forcing on the downstream structures. The pressure field analysis demonstrated pronounced static and dynamic pressure variations across the columns, confirming the unsteady nature of the aerodynamic loads. Regions of high dynamic pressure between cylinders were observed to coincide with low static pressure zones, producing alternating lift and drag forces.

Such periodic fluctuations are responsible for vortex-induced vibrations (VIV), which may lead to fatigue accumulation in offshore risers, tension-leg platforms, and turbine foundations if not adequately controlled. The present results align with earlier experimental observations, which reported similar oscillatory trends in multi-cylinder arrays, validating the numerical accuracy of the proposed CFD approach. Furthermore, the Reynolds number distributions and velocity profiles revealed the dependency of vortex formation on local flow acceleration and boundary layer separation. The localized peaks in Re upstream of the columns, followed by a rapid decrease downstream, indicate regions of shear layer detachment and reattachment that strongly affect the wake dynamics. The numerical results thus provide a realistic picture of transitional flow behavior within the subcritical regime ($Re \approx 10^4$), where laminar-to-turbulent transition occurs intermittently along the cylinder surfaces. From a structural dynamic's perspective, the findings highlight the importance of geometric configuration in mitigating unsteady flow effects.

Adjusting the spacing ratio (S/D) and angular alignment between columns can substantially reduce vortex synchronization, leading to lower amplitude vibrations. This observation supports design optimization strategies for offshore foundations, risers, and energy-harvesting systems, where preventing resonance and minimizing fatigue are crucial for long-term performance. Moreover, the ability of the CFD model to capture both steady-state pressure distributions and transient vortex shedding phenomena establishes a reliable computational framework for future parametric studies. The study also illustrates that turbulence modeling plays a significant role in the accuracy of flow predictions. While the realizable k–ε model effectively captured mean flow characteristics and general vortex structures, it exhibited limitations in resolving instantaneous vortex shedding and three-dimensional instabilities.

To further enhance accuracy, future analyses could employ Large Eddy Simulation (LES) or Detached Eddy Simulation (DES) to capture fine-scale turbulence dynamics that influence fatigue loading and resonance conditions.

Nevertheless, the current results show strong agreement with benchmark data, confirming that the chosen modeling approach provides a practical balance between computational efficiency and physical accuracy. Overall, the discussion underscores that vortex-induced vibrations are not solely determined by flow velocity or Reynolds number but also by the mutual interaction between structural geometry and fluid motion. The observed vortex synchronization, wake shielding, and periodic fluctuations in pressure and velocity collectively define the dynamic environment around offshore installations.

The insights derived from this study not only enhance understanding of fundamental fluid mechanics but also have direct engineering implications for designing stable and fatigue-resistant offshore systems operating under complex flow conditions.

5. CONCLUSION

The present investigation successfully developed and validated a computational fluid dynamics (CFD) model using ANSYS Fluent to analyze fluid–structure interactions around cylindrical obstacles representative of offshore structural elements.

A structured grid containing 63,699 cells was generated to ensure numerical stability and spatial resolution, and the mass conservation residuals demonstrated third-order accuracy, confirming the robustness and reliability of the adopted numerical framework. The analysis of flow characteristics revealed pronounced streamline deflection around the cylinders, accompanied by localized velocity peaks up to 22.4 m/s in the wake regions. These results were consistent with Bernoulli's principle, verifying that flow acceleration occurs where cross-sectional area decreases. Pressure contour maps showed substantial fluctuations in both static and dynamic pressure, ranging from 48.9 kPa to 3.98 kPa, as the flow interacted with the cylindrical obstacles. These fluctuations contributed directly to vortex shedding, which generated oscillatory loads responsible for vortex-induced vibrations (VIV)—a critical factor influencing the stability and fatigue life of marine structures. The findings further demonstrated that the amplitude and frequency of VIV are highly dependent on the spatial arrangement of cylindrical members.

Appropriate spacing and alignment were found to reduce destructive interference, thereby minimizing fatigue accumulation and enhancing the long-term durability of offshore installations.

This behavior holds particular importance for the design of wind turbine foundations, marine risers, and energy-harvesting systems, where mitigating flow-induced oscillations directly improves reliability and operational safety. Theoretical consistency was also confirmed across the computational results. The Reynolds number exhibited its peak values upstream of the cylinders, in agreement with analytical predictions, while the velocity magnitude contours reaffirmed Bernoulli's relationship by illustrating higher flow speeds through constricted passages. Furthermore, the negative order of magnitude observed in the mass conservation residuals underscored the high numerical precision and credibility of the developed CFD model. Overall, the study underscores the fundamental importance of fluid–structure interaction (FSI) in offshore engineering and provides meaningful insights for optimizing the hydrodynamic performance and structural resilience of marine systems.

While the present research offers a reliable CFD framework, it remains limited by the use of Reynolds-Averaged Navier–Stokes (RANS) turbulence modeling, which cannot fully capture transient and three-dimensional vortex dynamics. Future investigations should therefore adopt Large Eddy Simulation (LES) or Direct Numerical Simulation (DNS) techniques, combined with experimental validation, to achieve higher temporal resolution and improved accuracy in predicting unsteady flow–structure interactions.

REFERENCES

[1] P. Li, L. Gao, Y. Wang, Z. Liu, L. Zhu, T. Su, Y. Huang, and Y. Wang, "Experimental study on vortex-induced vibration of risers fitted with detached splitter plate vibration suppression and energy harvesting device," *Ocean Engineering*, vol. 320, p. 120318, Mar. 15, 2025, doi: 10.1016/j.oceaneng.2025.120318.

[2] A. Mohey, S. A. Ibrahim, H. M. Abdel-Khalek, and M. A. Barakat, "Examining the pedestrian-level wind environment around high-rise buildings using CFD simulations: Effect of height and shape," *IOP Conference Series: Earth and Environmental Science*, vol. 1530, 16th Int. Conf. on Civil and Architectural Engineering (ICCAE-16), Cairo, Egypt, May 12–15, 2025, p. 012013, doi: 10.1088/1755-1315/1530/1/012013.

[3] T. Stathopoulos, H. Wu, and C. Bédard, "Wind environment around buildings: A knowledge-based approach," *Journal of Wind Engineering and Industrial Aerodynamics*, vol. 44, nos. 1–3, pp. 2377–2388, Oct. 1992, doi: 10.1016/0167-6105(92)90028-9.

[4] Moradi, M., Saadat-Abadi, A. R., Fattahi, E., & Rahimzadeh, F. Assessment of Annual Wind Speed Homogeneity at Iranian Meteorological Stations (1981-2015). Journal of Meteorology and Atmospheric Sciences, 1(2), 146-162, 2018.

[5] Karadag, I., & Yuksek, I. Turkey Wind Turbine Integration to Tall Buildings (Doctoral dissertation). Manisa Celal Bayar University, Manisa, 2020. http://dx.doi.org/10.5772/intechopen.91650

[6] S. A. Abdollahi, S. F. Ranjbar, M. Jafarai, M. B. Ehghaghi, and S. Faramarzi, "Enhancing wind energy efficiency: A study on the power output of shrouded wind turbines for a hydrogen storage system," *Results in Engineering*, vol. 26, p. 104710, Jun. 2025, doi: 10.1016/j.rineng.2025.104710.

[7] P. Kumar and S. K. Singh, "Flow past a bluff body subjected to lower subcritical Reynolds number," *Journal of Ocean Engineering and Science*, vol. 5, no. 2, pp. 173–179, Jun. 2020, doi: 10.1016/j.joes.2019.10.002

[8] B. Fu and D. Wan, "Numerical study of vibrations of a vertical tension riser excited at the top end," *Journal of Ocean Engineering and Science*, vol. 2, no. 4, pp. 268–278, Dec. 2017, doi: 10.1016/j.joes.2017.09.001.

[9] S. Muddada, K. Hariharan, V. S. Sanapala, and B. S. V. Patnaik, "Circular cylinder wakes and their control under the influence of oscillatory flows: A numerical study," *Journal of Ocean Engineering and Science*, vol. 6, no. 4, pp. 389–399, Dec. 2021, doi: 10.1016/j.joes.2021.04.002.

[10] D. Sumner, "Two circular cylinders in cross-flow: A review," *Journal of Fluids and Structures*, vol. 26, no. 6, pp. 849–899, Aug. 2010, doi: 10.1016/j.jfluidstructs.2010.07.001.

[11] Jafari, A. Design, Fabrication, and Testing of Electricity-Generating Wind Turbines (Master's thesis). Shiraz University, Department of Mechanical Engineering, 1999.

[12] F. J. Huera-Huarte, Z. A. Bangash, and L. M. González, “Multi-mode vortex and wake-induced vibrations of a flexible cylinder in tandem arrangement,” *Journal of Fluids and Structures*, vol. 66, pp. 571–588, Oct. 2016, doi: 10.1016/j.jfluidstructs.2016.07.019.

[13] X. Fan, Z. Wang, Y. Wang, and W. Tan, “The effect of vortices structures on the flow-induced vibration of three flexible tandem cylinders,” *International Journal of Mechanical Sciences*, vol. 192, p. 106132, Feb. 15, 2021, doi: 10.1016/j.ijmecsci.2020.106132.

[14] A. Bakhtiari, M. Zeinoddini, H. Ashrafipour, V. Tamimi, M. M. A. Harandi, and P. Jadidi, “The effects of marine fouling on the wake-induced vibration of tandem circular cylinders,” *Ocean Engineering*, vol. 216, p. 108093, 2020, doi: 10.1016/j.oceaneng.2020.108093.

[15] W. Xu, Y. Ma, A. Cheng, and H. Yuan, “Experimental investigation on multi-mode flow-induced vibrations of two long flexible cylinders in a tandem arrangement,” *International Journal of Mechanical Sciences*, vol. 135, pp. 261–278, 2018, doi: 10.1016/j.ijmecsci.2017.11.027.

[16] S. Huang and A. Sworn, “Hydrodynamic coefficients of two fixed circular cylinders fitted with helical strakes at various staggered and tandem arrangements,” *Applied Ocean Research*, vol. 43, pp. 21–26, 2013, doi: 10.1016/j.apor.2013.06.001.

[17] K. Lin, D. Fan, and J. Wang, “Dynamic response and hydrodynamic coefficients of a cylinder oscillating in crossflow with an upstream wake interference,” *Ocean Engineering*, vol. 209, p. 107520, 2020, doi: 10.1016/j.oceaneng.2020.107520.

[18] I. Korkischko and J. R. Meneghini, “Experimental investigation of flow-induced vibration on isolated and tandem circular cylinders fitted with strakes,” *Journal of Fluids and Structures*, vol. 26, no. 4, pp. 611–625, 2010, doi: 10.1016/j.jfluidstructs.2010.03.001.

[19] G. R. S. Assi, J. R. Meneghini, J. A. P. Aranha, P. W. Bearman, and E. Casaprima, “Experimental investigation of flow-induced vibration interference between two circular cylinders,” *Journal of Fluids and Structures*, vol. 22, nos. 6–7, pp. 819–827, 2006, doi: 10.1016/j.jfluidstructs.2006.04.013.

[20] Evaluation of Wind Energy Potential and Feasibility Study of Wind Power Plant Construction in Sabzevar. Entezari, M. Studies of Geographic Areas of Dry Regions, Year 3, Numbers 9 and 10, Autumn and Winter 2012.

[21] N. Shambira, P. Mukumba, and G. Makaka, “Assessing the wind energy potential: A case study in Fort Hare, South Africa, using six statistical distribution models,” *Applied Sciences*, vol. 15, no. 5, p. 2778, Mar. 5, 2025, doi.org/10.3390/app15052778.

[22] S. Filom, S. Radfar, R. Panahi, E. Amini, and M. Neshat, “Exploring wind energy potential as a driver of sustainable development in the southern coasts of Iran: The importance of wind speed statistical distribution model,” *Sustainability*, vol. 13, no. 14, p. 7702, Jul. 9, 2021, doi.org/10.3390/su13147702.

[23] M. Bošnjaković, M. Martinović, and K. Đokić, “Application of artificial intelligence in wind power systems,” *Applied Sciences*, vol. 15, no. 5, p. 2443, Feb. 25, 2025, doi.org/10.3390/app15052443.

[24] M. Bousla, M. Belfkir, A. Haddi, Y. El Mourabit, and A. Sadki, “Comparative evaluation of Weibull parameter estimation methods for wind energy forecasting: A case study of the Tetouan wind farm with SCADA-based availability integration,” *Results in Engineering*, vol. 27, p. 106835, Sep. 2025, doi.org/10.1016/j.rineng.2025.106835.

[25] Renewable Energy Organization of Iran (SANAE). (2012). Retrieved from http://www.sana.ir

[26] G. Roshan, M. S. Najafi, Á. M. Costa, and J. A. Orosa, “Effects of climate change on wind energy production in Iran,” *Arabian Journal of Geosciences*, vol. 8, no. 4, Mar. 2014, doi: 10.1007/s12517-014-1374-2.

[27] M. Azizi and A. Jahangirian, “Multi-site aerodynamic optimization of wind turbine blades for maximum annual energy production in East Iran,” *Energy Science & Engineering*, vol. 8, no. 6, Feb. 2020, doi: 10.1002/ese3.656.

[28] Q. Ai, P. M. Weaver, T. K. Barlas, A. S. Olsen, H. A. Madsen, and T. L. Andersen, “Field testing of morphing flaps on a wind turbine blade using an outdoor rotating rig,” *Renewable Energy*, vol. 133, pp. 53–65, Apr. 2019, doi: 10.1016/j.renene.2018.09.092.

[29] M. McWilliam, T. Barlas, H. A. Madsen, and F. Zahle, “Aero-elastic wind turbine design with active flaps for AEP maximization,” *Wind Energy Science Discussions*, Nov. 2017, doi: 10.5194/wes-2017-50.

[30] A. Saenz-Aguirre, U. Fernandez-Gamiz, E. Zulueta, I. Aramendia, and D. Teso-Fz-Betono, “Flow control based 5 MW wind turbine enhanced energy production for hydrogen generation cost reduction,” *International Journal of Hydrogen Energy*, vol. 47, no. 11, pp. 7049–7061, Feb. 5, 2022, doi: 10.1016/j.ijhydene.2020.01.022.

[31] Y. Zhang, V. Ramdoss, Z. Saleem, X. Wang, G. Schepers, and C. Ferreira, "Effects of root Gurney flaps on the aerodynamic performance of a horizontal axis wind turbine," *Energy*, vol. 187, p. 115955, Nov. 15, 2019, doi: 10.1016/j.energy.2019.115955.

[32] E. Branlard, *Wind Turbine Aerodynamics and Vorticity-Based Methods: Fundamentals and Recent Applications*, vol. 7 of *Research Topics in Wind Energy*. Cham, Switzerland: Springer, 2017.

[33] J. E. Cermak, "Wind environment: Theme introduction and report on preprint papers not included in proceedings," *Advances in Wind Engineering*, pp. 99–103, 1988, doi: 10.1016/B978-0-444-87156-5.50019-9.

[34] Y. Li and L. Chen, "Study on the influence of voids on high-rise building on the wind environment," *Building Simulation*, vol. 13, pp. 419–438, 2020, doi.org/10.1007/s12273-019-0584-7.

[35] M. Gür and I. Karadag, "Machine learning for pedestrian-level wind comfort analysis," *Buildings*, vol. 14, no. 6, p. 1845, Jun. 18, 2024, doi: 10.3390/buildings14061845.